Damage-free atomic layer etching process

The optical microscopic images of WSe_2 for each step enabling atomic layer etching (ALE) process are shown in Fig. S1a. 1L-WSe_2 becomes barely visible after UV-ozone treatment due to formation of tungsten oxyselenide (TOS) while 2L and 4L are still clearly visible indicating underlying layers are not oxidized. The surface of sample is cleaned and flattened by eliminating residues after oxidation as shown in Fig. S1b. After a KOH rinse for 10-seconds, each flake is one-layer thinned (e.g. 2L becomes 1L). It is indicative of self-limited oxidation (only topmost layer is oxidized) and damage-free etching. Fig. S1c shows the four-probe measurements for each step. For the as-fabricated device, the Dirac point is at back-gate bias (V_{GS}) = +30 V; while it completely disappears from the measurement range after oxidation implying degenerate doping effect. It is noted that the TOS doesn't contributed to the carrier transport as Fig. S4 shows no noticeable current after UV-ozone oxidation. The device is characterized again after the TOS-doping layer is removed using a 10-second potassium hydroxide (KOH) dip followed by a vacuum anneal at 300 ˚C for 30 minutes that eliminates solvent residue. After removal of the TOS layer, the electrical characteristics of pristine graphene are recovered with a Dirac point at ~0 V. It motivates our high-quality doping technique using TOS by UV-ozone treatment. These steps can be repeated a few more cycles for clean ALE process.

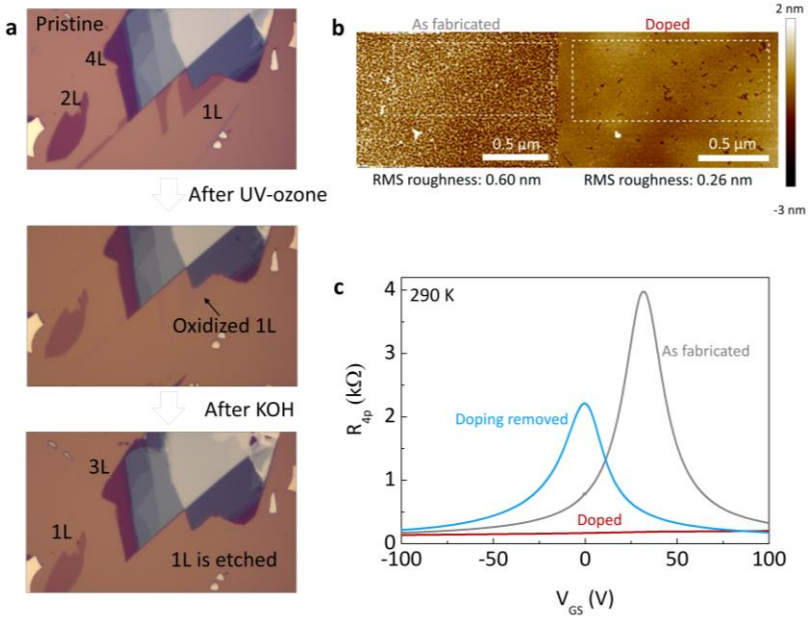

Figure S1 | Demonstration of atomic layer etching. **a**, Optical microscopic images of WSe_2 with different thicknesses for pristine, after UV-ozone and after KOH. **b**, Atomic force microscopic images for WSe_2/Gr before and after oxidation. **c**, Electrical characterization of WSe_2 at each step.

Electrical characterizations for TOS and TOS-doped graphene

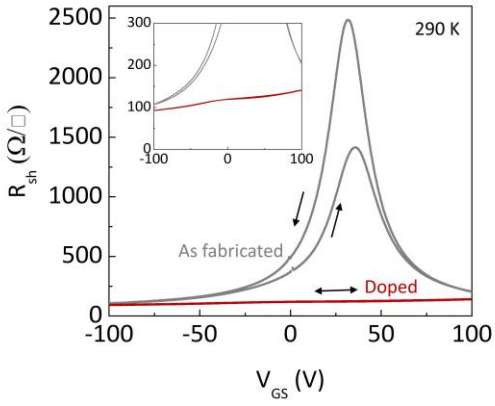

Figure S2 | Hysteresis of a 1L-WSe_2/Gr device before and after UV-ozone. Double swept transfer curves of as-fabricated and doped a 1L-WSe_2/Gr device measured at 290 K. Hysteresis is negligible after doping due to a surface cleaning effect by UV-ozone treatment.

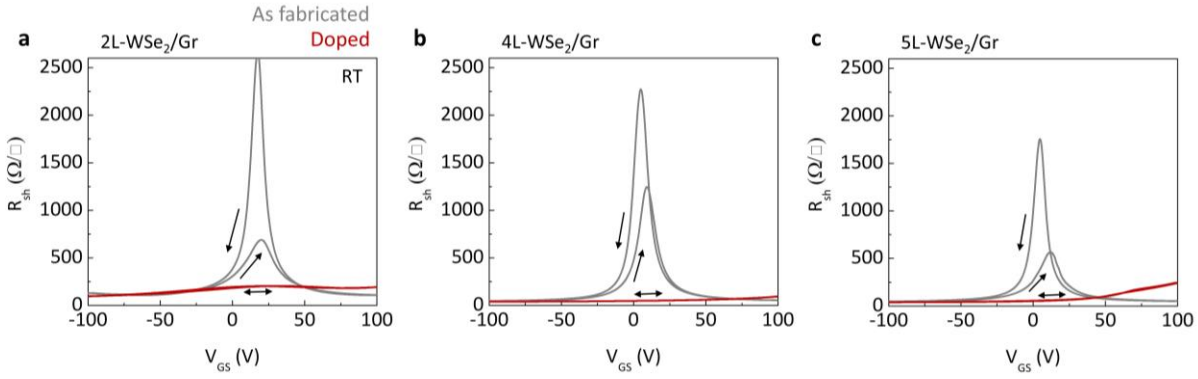

Figure S3 | Transfer curves for graphene devices with WSe_2 interlayers. Transfer curves for graphene devices with **a**, 2L-WSe_2, **b**, 4L-WSe_2, and **c**, 5L-WSe_2 interlayers before and after doping.

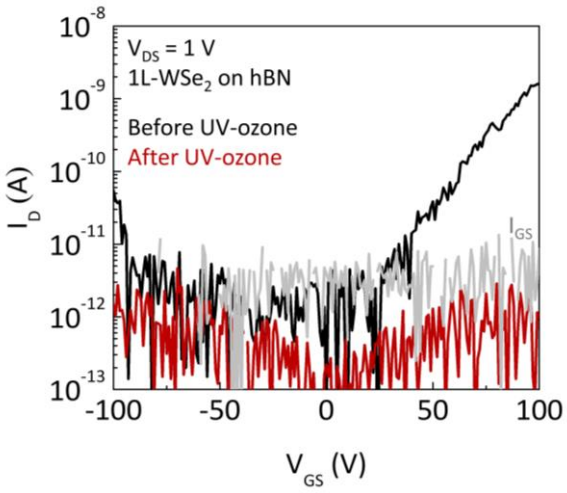

Figure S4 | Transfer curves of a 1L-WSe_2 device. Transfer curves of a 1L-WSe_2 device before and after UV-ozone at V_{DS} = 1 V. The Cr/Au contacts were formed by the edge contact method used for graphene devices. It shows an n-type semiconducting behavior before doping and the current drops to the noise floor of our measurement system (gray line indicates the leakage current, I_{GS}) after doping.

TEM and EDS measurements

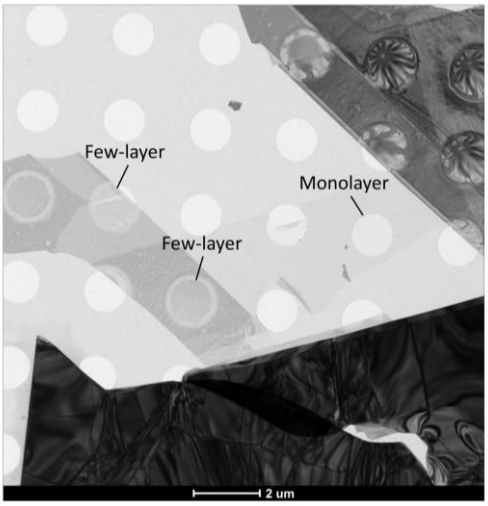

Figure S5 | Transmission electron microscopy (TEM). TEM image for monolayer and few-layer WSe_2 used for selected area electron diffraction patterns.

Atomic percentage of 1L-WSe_2 from EDS						
	C	W	Se	O	Se/W	O/W
Pristine	98.87	0.25	0.72	0.17	2.88	0.68
Oxidized	94.87	0.55	0.38	4.2	0.69	7.64

Table S1 |Atomic percentage of monolayer WSe_2 from EDS. The table shows the obtained atomic percentage of C, W, Se, O atoms, and Se/W and O/W ratio for monolayer WSe_2 from EDS. It is noted that the atomic ratio of Se/W for monolayer is significantly reduced (although not completely removed) while O/W ratio increases by the oxidation process, indicating that the Se atoms are mostly replaced by oxygen atoms.

Fig. S5 shows TEM images for monolayer and few-layer WSe_2 for SAED patterns in main manuscript. Table S1 is atomic percentage of monolayer WSe_2 before and after UV-ozone treatment obtained by EDS. The atomic ratio of Se/W is significantly reduced while O/W ratio is increased (although Se is not completely removed and therefore, denoted as TOS) by the oxidation process. Negligible hysteresis in the transfer curves after UV-ozone in Figs. S2 and S3 further corroborates our claim of a clean surface and self-limiting nature. With this damage-free oxidation process accompanied by a clean surface, TOS provides high-quality doping with remarkably high mobility and low sheet resistance as shown in Fig. S9 and mobility comparison of Fig. 3 in the main manuscript.

PMMA passivation effect

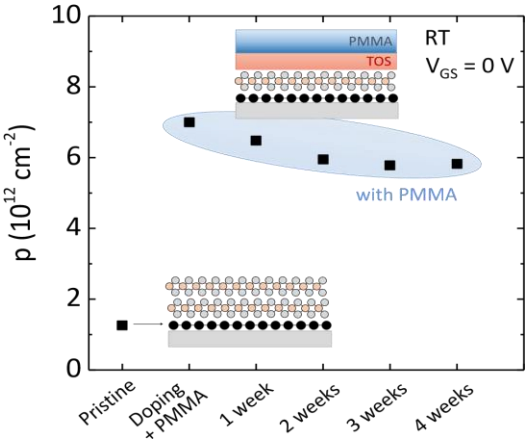

Figure S6 | Passivation effect by PMMA deposition. p at V_{GS} = 0 V for PMMA covered TOS-doped graphene measured at RT. It shows a slight reduction of carrier density from 7 to 6 × 10^{12}cm^{-2} after 4 weeks of measurements.

Carrier density and Hall mobility extraction

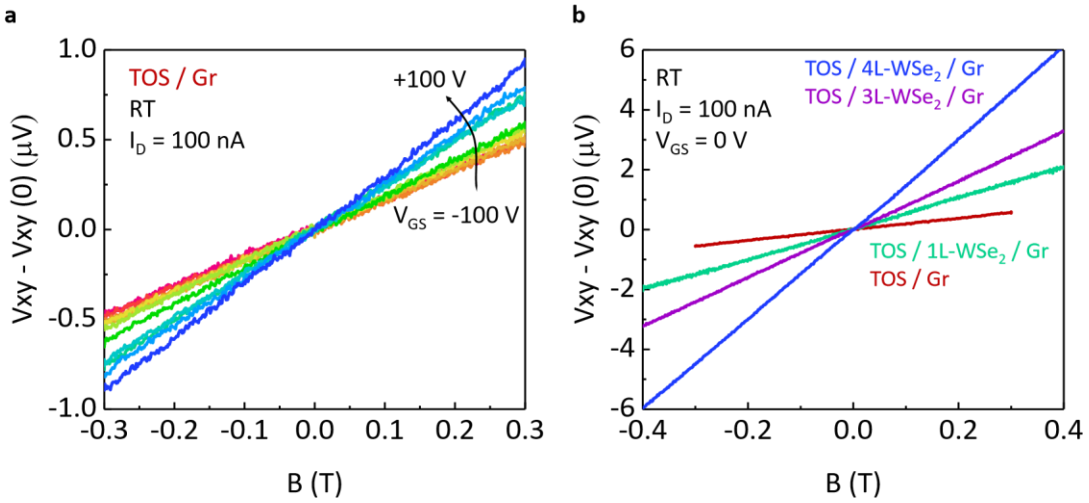

Figure S7 | Normalized Hall voltage as a function of B-field for TOS-doped graphene. **a**, Normalized V_{xy} as a function of B-field for graphene with 1L-TOS at different V_{GS}. **b**, Normalized V_{xy} as a function of B-field for TOS-doped graphene with and without WSe_2 interlayers at zero V_{GS}.

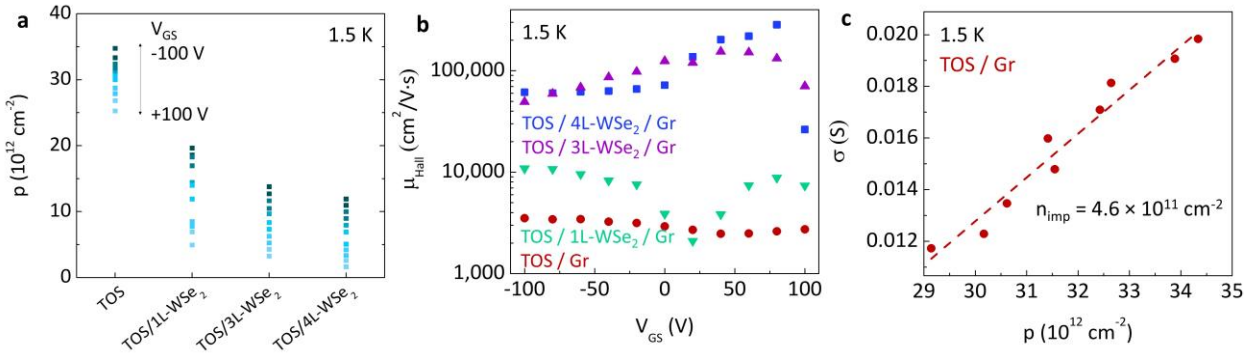

Figure S8 | Low temperature (1.5 K) measurements for TOS-doped graphene. **a**, p and **b**, μ_{Hall} for TOS-doped graphene with 0, 1, 3, 4L-WSe_2 interlayers at 1.5 K. The hole densities show similar values to those obtained at 290 K. μ_{Hall} improves comparing to RT measurements due to a reduced phonon scattering. **c**, σ as a function of p for TOS-doped graphene without WSe_2 interlayer. The impurity density n_{imp} of 4.6 × 10^{11} cm^{-2} is estimated from the slope of the plot.

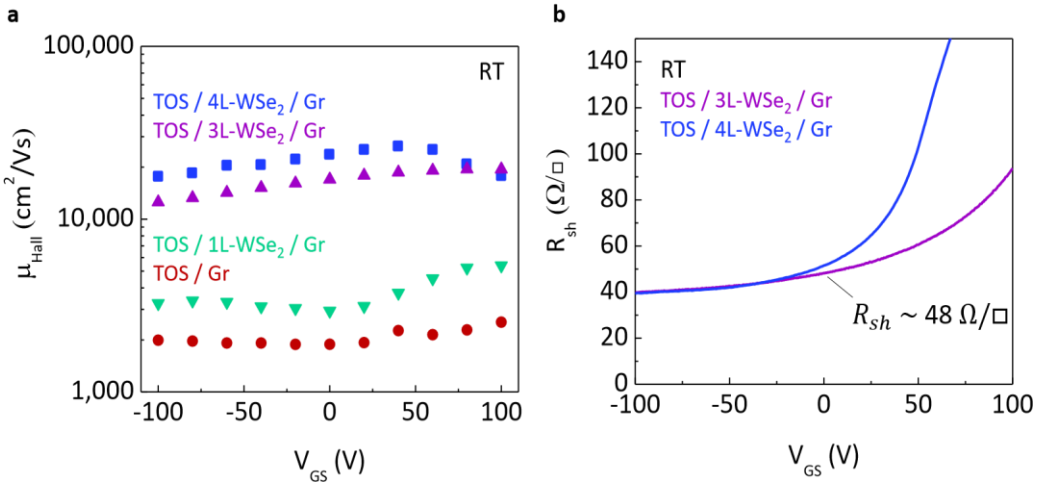

Figure S9 | Hall mobility and sheet resistance for TOS-doped graphene. **a**, μ_{Hall} and **b**, R_{sh} vs. V_{GS} at RT. With 3L- and 4L-WSe_2 interlayers, μ_{Hall} is > 10,000 $cm^2/(V \cdot s)$ and R_{sh} is ~50 Ω/sq.

Thickness of thin *h*-BN measured by AFM

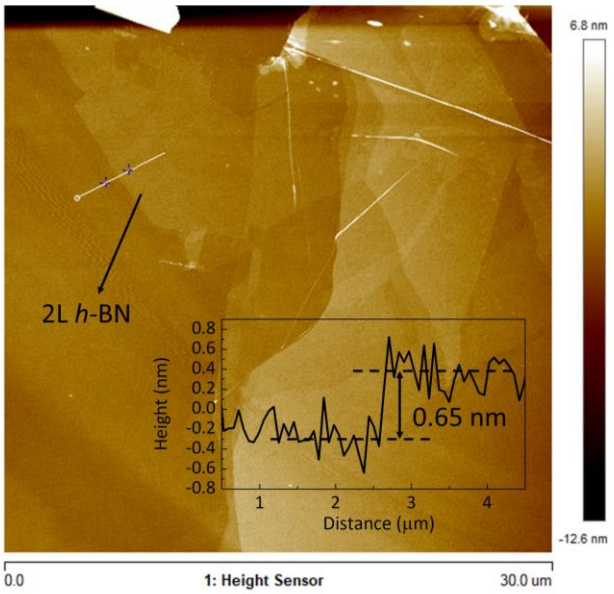

Figure S10 | Thickness of 2L *h*-BN (~0.65 nm) confirmed by AFM as shown in the line profile for TOS/*h*-BN/Gr sample used in Raman map in Fig. 4b.

Universal doping effects of TOS

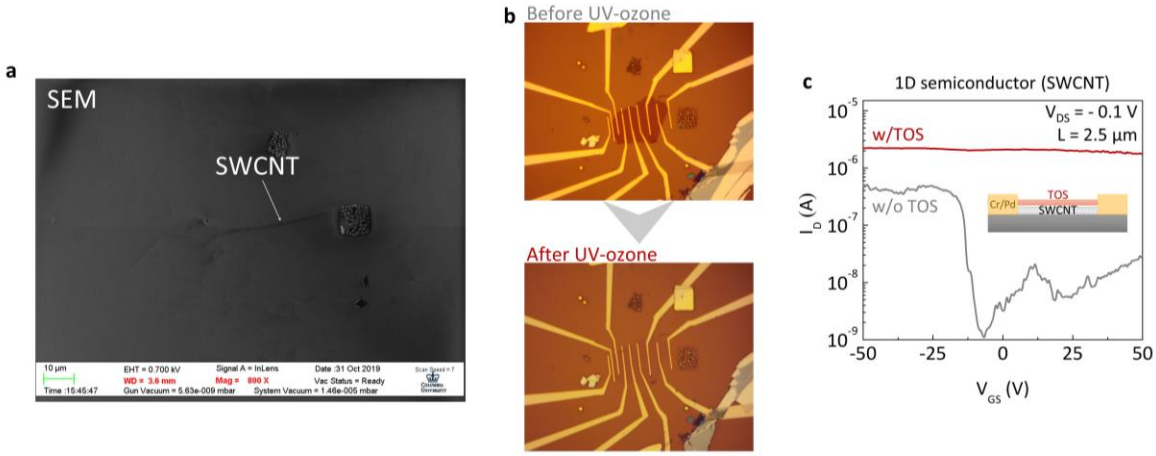

Figure S11 | TOS doping effects on a SWCNT device. **a**, SEM image to show a SWCNT grown from a metal seed. **b**, Optical microscopic images for the fabricated device based on the position of SEM image with transferred WSe_2. After UV-ozone, the WSe_2 became barely visible indicating a formation of TOS layer. **c**, Transfer characteristics for SWCNT device with and without 1L-TOS.

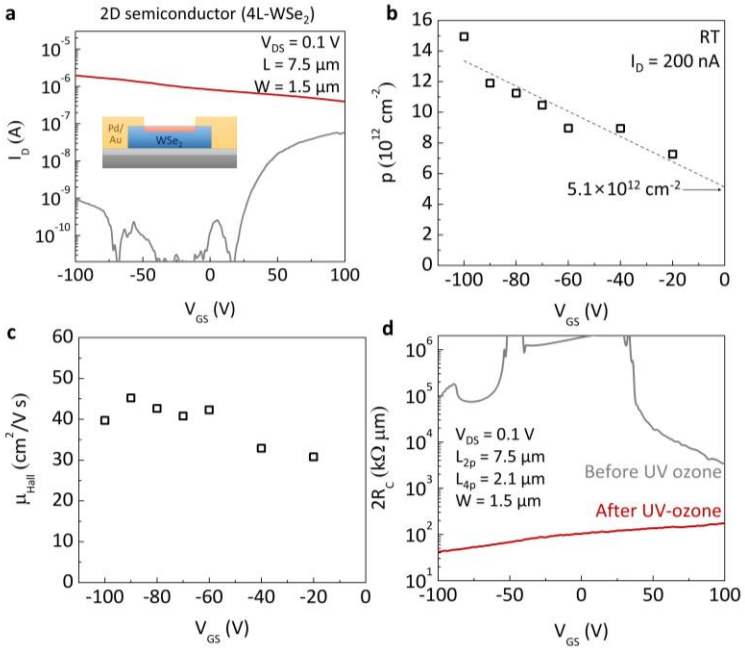

Figure S12 | Electrical characterization of TOS-doped WSe_2. **a**, I_D, **b**, p and **c**, μ_{Hall} vs. V_{GS} for a doped 4L-WSe_2 device. The channel layer became 3L since topmost layer became TOS after UV-ozone treatment. p vs. V_{GS} shows approximately linear behavior and $p = 5.1 \times 10^{12}$ cm^{-2} at $V_{GS} = 0$ V. **d**, $2R_c$ vs. V_{GS} at $V_{DS} = 0.1$ V before and after UV-ozone. R_c is decreased by at least 20-fold due to the doping effect.

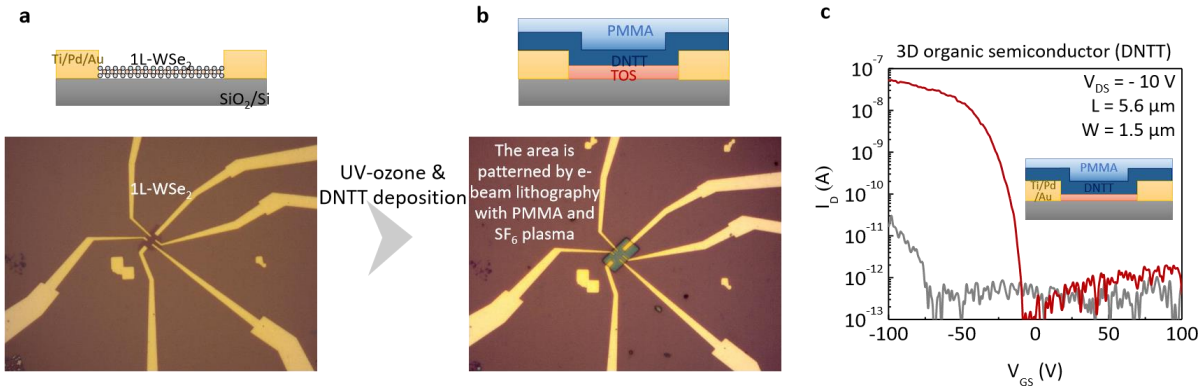

Figure S13 | TOS doping effects on a DNTT device. **a**, 1L-WSe_2 was prepared on a SiO_2/Si substrate by mechanical exfoliation followed by metallization. **b**, After UV-ozone treatment, DNTT layer was deposited by sublimation. To define the channel area, it was patterned by e-beam lithography following SF_6 plasma etching. PMMA layer for the patterning was not removed to protect the channel organic layer. **c**, Transfer characteristics for DNTT devices with and without 1L-TOS.

Electrostatic simulation of TOS-doped Gr with WSe_2 interlayers

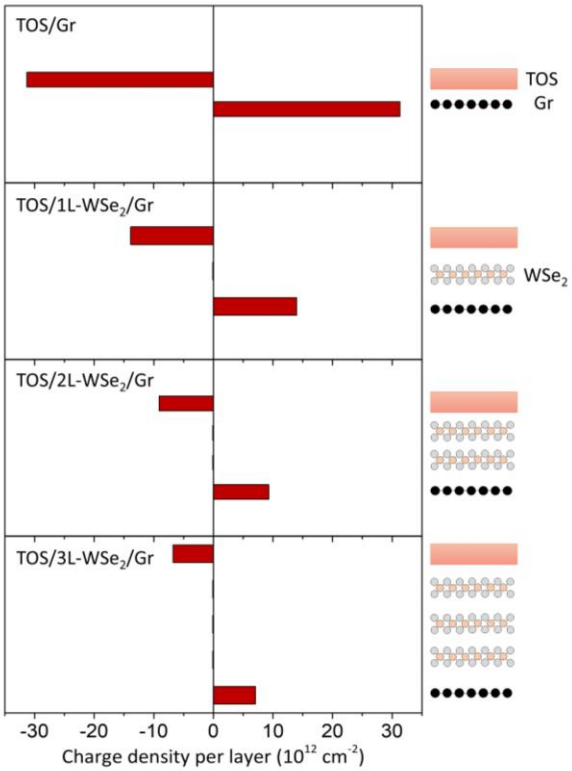

Figure S14 | Self-consistent electrostatic simulation of induced charge density in TOS-doped graphene for different thickness of WSe_2 interlayer.

Bandgap (E_G)	Electron affinity (χ)	Effective electron mass (m_e^*)	Effective hole mass (m_h^*)
2.08	3.53	0.48	0.44

Table S2| Additional material parameters for WSe_2 used for self-consistent electrostatic simulations.

Transmittance measurements for TOS-doped graphene

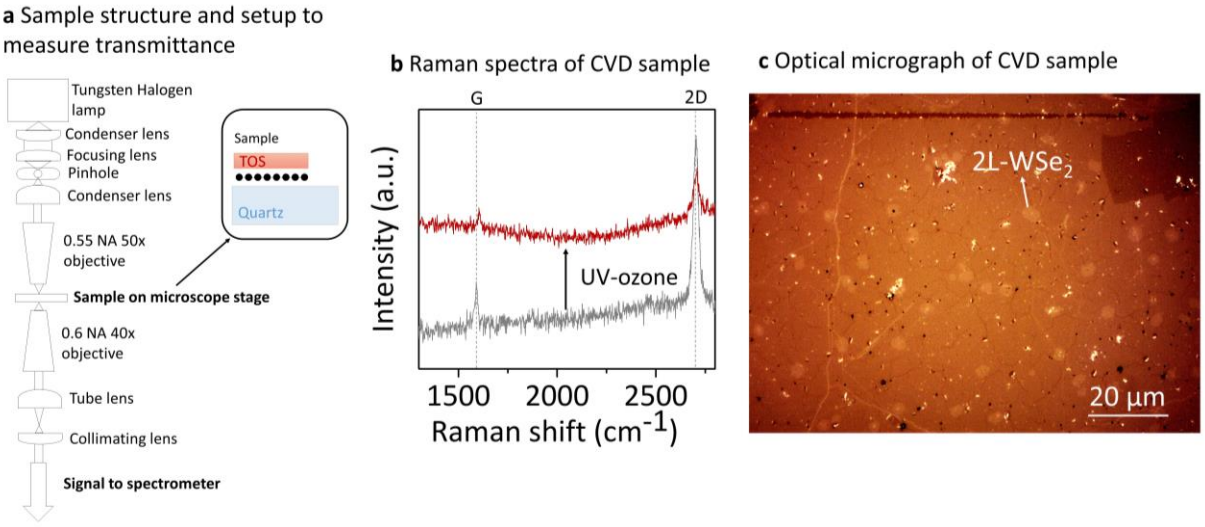

Figure S15 | Transmittance measurement setup, Raman spectra, and optical image for CVD sample. **a**, Measurement setup for transmittance. **b**, Raman spectra of CVD grown 1L-WSe_2 on graphene before and after UV-ozone. Similar blue-shifts of G and 2D bands are observed to the exfoliated sample. **c**, Optical microscopic image of CVD sample shows some part of 2L-WSe_2.

Optical loss measurements with SIN photonic waveguides

I. Normalized Ring Transmission vs. wavelength for composite WSe_2 (TOS)/Gr/*h*-BN on SiN photonic waveguides

We show here the experimentally obtained ring transmission spectra as a function of wavelength with different configurations of the SiN composite waveguide. We first measure the normalized transmission spectra of the bare SiN planarized waveguides (in blue), embedded in the ring resonator configuration. In this configuration, the gap between the bus waveguide and the ring

resonator is 450 nm and remains the same for other measurements. One can see from the blue spectra in Fig. S16, that the SiN only resonance spectra exhibit low extinction ratio and narrow linewidth, which implies that the device is initially in the under-coupled regime, where the propagation loss in the ring is considerably lower than the coupling rate between the bus waveguide and the ring resonator.

After the transfer of WSe_2/Gr/*h*-BN stack on top of SiN waveguides in the ring cavity, we measure the normalized transmission spectra of the ring resonator with a portion of the ring (25 – 30 µm) with the composite waveguide (grey spectra in Fig. S16). We observe that not only does the resonance wavelength blue shifts, but also the linewidth broadens considerably with low extinction. The blue shift in the resonance wavelength is due to the modification of the effective refractive index in a ring resonator, due to the change in the waveguide cladding of WSe_2/Gr/*h*-BN. We can attribute the linewidth broadening to the lossy graphene on the SiN waveguide. In this configuration, the ring is in the over-coupled regime, where the loss (decay rate) in the ring is higher than the coupling rate.

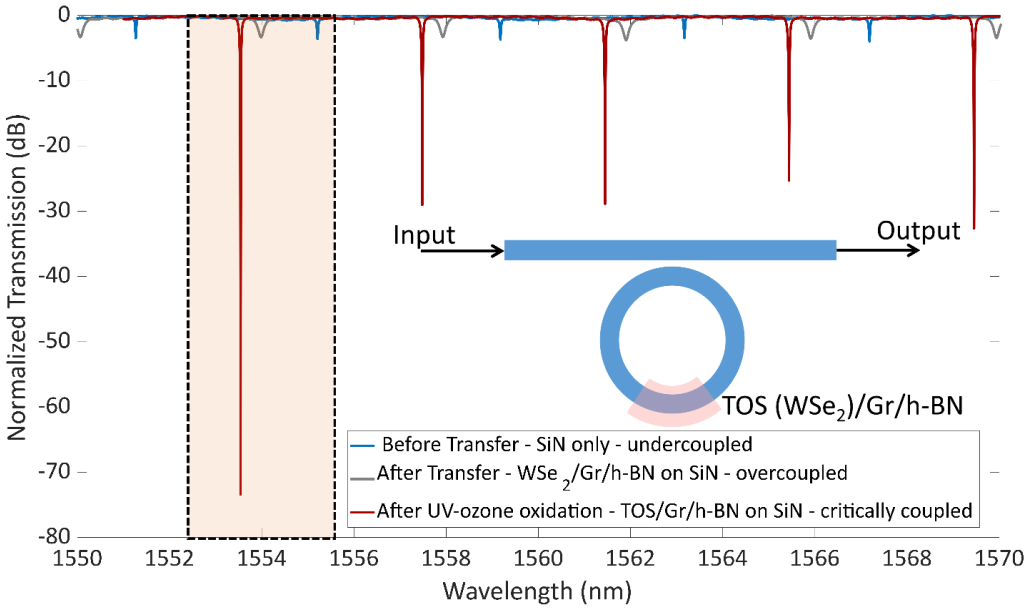

Figure S16 | Normalized transmission response of microring resonator with SiN composite waveguide. Inset shows the schematic of the microring resonator of radius (R) 50 µm with a 25-30 µm long TOS(WSe_2)/Gr/*h*-BN stack on the ring resonator. One can see from the normalized transmission response that the multiple resonances are separated by the free spectral range (FSR) given by the effective index of the propagating light and the cavity length ($L = 2\pi R$). For the purposes of our main paper figure, we concentrate on the transmission response shown in the shaded region.

Finally, UV-ozone oxidation of monolayer WSe_2 in our sample causes the graphene to reach doping densities exceeding 2.5×10^{13} cm^{-2} for the composite TOS/Gr/*h*-BN on SiN waveguides. We measure the normalized ring transmission as seen in the red spectra of Fig. S16 and find that the ring resonance further blue shifts and the device reaches the critically coupled condition with maximum extinction and narrow linewidth. The critical coupling condition is achieved when the decay rate due to loss in the ring equals the coupling rate between the input bus waveguide and the ring resonator. We attribute the decrease in loss and linewidth narrowing from the grey spectra to the doped graphene, which leads to Pauli blocking at the resonance wavelength of 1553.54 nm. The limit in the percent of reduction in loss in doped graphene is limited by the intraband absorption at high carrier densities.

II. Estimation of insertion loss due to doped and undoped graphene in the composite WSe_2(TOS)/Gr/*h*-BN - SiN photonic waveguides

We estimate the insertion loss of the propagating mode by numerically fitting the normalized ring transmission to the theoretical transmission (T) obtained using the following equation,

$$T = \left| 1 - \frac{\frac{2}{\tau_e}}{j(\omega - \omega_0) + \frac{1}{\tau_0} + \frac{1}{\tau_e}} \right|^2,$$

where ω_0 is the resonant frequency, $\frac{1}{\tau_0}$ is the decay rate due to loss, $\frac{1}{\tau_e}$ is the decay rate from the bus to ring resonator (coupling rate). The decay rates are related to the unloaded quality factor Q_0 by the equation $Q_0 = {\omega_0 \tau_0}/{2}$.

The condition for critical coupling states that the decay rate due to loss should match the decay rate from the bus to ring resonator such that, $\frac{1}{\tau_{0\_CC}} = \frac{1}{\tau_e}$. Under this condition, at the resonant frequency (ω_0) with zero detuning, the transmission reaches the regime of maximum extinction. We observe that our device reaches the critical coupling regime when the graphene is doped. Leveraging the red spectra, one can fit the T and compute τ_e, which remains a constant since we use the same device for the other two measurements. In the case of bare SiN planarized waveguide, we are in the regime of under coupling where that $\tau_{0\_UC} > (\tau_e = \tau_{o\_CC})$. For the regime of over-coupling with undoped graphene covering a portion of the ring, the lifetimes are related by $(\tau_{o\_OC} < \tau_{o\_CC} = \tau_e)$.

The insertion loss in dB (α_{dB}) is related to the unloaded quality factor Q_0 by $\alpha_{dB} = \frac{2\pi n_g}{Q\lambda_0} \times (20 \log_{10} e)$, where n_g is the group index extracted from the transmission spectra in Fig. S16. The n_g is related to the FSR ($\Delta\lambda = \lambda_m - \lambda_{m+1}$) by $n_g = \frac{\lambda_m \lambda_{m+1}}{2\pi R \Delta\lambda}$, where λ_m denotes the mth resonance and R is the radius of the ring.

From fitting the undercoupled spectra of Fig. S16 with theoretical transmission (T), we estimate that the propagation loss in bare SiN waveguide is 2.326 dB/cm. After transfer of 25-30 μm long WSe_2/Gr/*h*-BN, the fitting estimates a propagation loss of 0.0770 dB/μm ± 18% with the composite waveguide. Finally, after UV-ozone oxidation, we find that the propagation loss of the composite waveguide is lowered to 0.012 dB/μm ± 18%. The error bar in our insertion loss estimation arises from the uncertainity in the length of the stack on the ring resonator.